



Palladium chalcogenide nanosheets with p-d orbital hybridization for enhanced alcohol electro-oxidation performance

Liping Wang^a, Zhiyong Yu^a, Wei Yan^a, Liangbin Liu^b, Mengjun Wang^a, Qingyu Kong^c, Zhiwei Hu^d, Hongbo Geng^e, Xiaoqing Huang^{a,b,*}, Yunhua Li^{a,**}

^a State Key Laboratory of Physical Chemistry of Solid Surfaces, College of Chemistry and Chemical Engineering, Xiamen University, Fujian 361005, China

^b Innovation Laboratory for Sciences and Technologies of Energy Materials of Fujian Province (IKKEM), Fujian 361005, China

^c Synchrotron Soleil, L'Orme des Merisiers, St-Aubin, Gif-sur-Yvette 91192 CEDEX, France

^d Max Planck Institute for Chemical Physics of Solids, Nothnitzer Strasse 40, Dresden 01187, Germany

^e School of Materials Engineering, Changshu Institute of Technology, Jiangsu 215500, China

ARTICLE INFO

Keywords:

Chalcogenide

C1 pathway selectivity

P-d orbital hybridization

C-C bond cleavage

Alcohol oxidation reaction

ABSTRACT

Ethanol oxidation reaction (EOR) is an important energy conversion process. Herein, we have proposed palladium chalcogenide nanosheets to improve C-C bond cleavage ability for EOR. The mass activity of the Te-Pd nanosheets (NSs)/C, which is higher than Se-Pd NSs/C and S-Pd NSs/C (6.9 A mg^{-1} and 5.3 A mg^{-1}), has achieved 10.0 A mg^{-1} , 12.5-fold higher than commercial Pd/C (0.8 A mg^{-1}) and 8.3 times higher than Pd NSs/C (1.2 A mg^{-1}). The Faradaic efficiency of C1 pathway for EOR on the Te-Pd NSs/C can improve to 56.6% compared with Pd NSs/C (25.7%) at $0.8 V_{\text{RHE}}$. Density functional theory calculations reveal that the orbital hybridization between Pd and Te weakens the adsorption energy of intermediates and reduces the energy barrier of the rate-determining steps in the C1 pathway. Besides, these palladium chalcogenide NSs can also serve as efficient electrocatalysts for ethylene glycol oxidation reaction and methanol oxidation reaction.

1. Introduction

Direct ethanol fuel cells (DEFCs) are critical for safe energy conversion and storage [1–3]. Among them, the complete oxidation of ethanol to carbon dioxide can release higher energy due to transferring $12 e^-$ (C1 pathway) [4,5]. However, ethanol oxidation reaction (EOR) requires overcoming a high energy barrier to break the C-C bond, which slows down the reaction kinetics of EOR. In contrast, the path to acetate generation only needs to transfer $4 e^-$ (called as C2 pathway). By comparison with C1 pathway, ethanol electro-oxidation easily occurs via C2 pathway to obtain acetate rather than CO_2 and CO_3^{2-} . Electrocatalysts with insufficient activity and low C1 pathway selectivity have restricted the development of DEFCs [3,6]. Ethylene glycol oxidation reaction (EGOR) and methanol oxidation reaction (MOR) also have the similar situation [7–9]. Therefore, Synthesizing catalysts with high catalytic activity and excellent C-C bond cleavage ability is essential for alcohol electro-oxidation performance.

Palladium (Pd) is considered the most promising alternative to Pt

due to its relatively more affluent reserves and the same number of valence electrons as Pt. However, the electrocatalytic performance of traditional Pd nanomaterials is still not ideal, especially for high C1 pathway selectivity, because of the intrinsic electronic structure of Pd [6,10–12]. To address this problem, great efforts have been made to synthesize Pd-based catalysts in EOR, such as modulating the Pd nanomaterial size, morphology (nanocube, nanowire, and nanoparticle), phase (rhombohedral Pd_3Sb_3 and fcc-2H-fcc heterophase) and alloy composition (containing Au, Rh, Pt, Ni and Cu) [6,13–25]. Even so, the C2 pathway still dominates the oxidation process of alkaline alcohols due to improper intermediates adsorption on active sites [26–29].

Compared with metallic elements, the doping of oxophilic non-metallic (NM) atoms, such as chalcogenide (S, Se and Te), can not only adjust the adsorption energy of intermediates, promoting the oxidation of carbon monoxide, but also modulate the electronic structure of Pd, enhancing cleavage ability of C-C bond [6,7]. Chemicals containing NM elements are cheap and easy to obtain [30–32]. Hence, NM-Pd electrocatalyst has been exploited in ethanol electro-oxidation.

* Corresponding author at: State Key Laboratory of Physical Chemistry of Solid Surfaces, College of Chemistry and Chemical Engineering, Xiamen University, Fujian 361005, China.

** Corresponding author.

E-mail addresses: [hxq006@xmu.edu.cn](mailto:hqx006@xmu.edu.cn) (X. Huang), yunhuali@xmu.edu.cn (Y. Li).

<https://doi.org/10.1016/j.apcatb.2023.123564>

Received 1 September 2023; Received in revised form 15 November 2023; Accepted 24 November 2023

Available online 29 November 2023

0926-3373/© 2023 Elsevier B.V. All rights reserved.

However, there is still a dearth of systematic investigation on efficient chalcogenides-doped Pd nanosheets in alcohol electro-oxidation.

Herein, we have successfully synthesized chalcogenide surface-doped Pd NSs via a two-step approach, which significantly enhance the electrochemical activity and the cleavage ability of C-C bond towards EOR in an alkaline solution. The mass activity (specific activity) of NM-Pd NSs/C is higher than commercial Pd/C and Pd NSs/C. In addition, the X-ray photoelectron spectroscopy (XPS) and X-ray absorption spectroscopy (XAS) results demonstrate that EOR performance improves due to the more exposed Pd active sites from the interaction between Pd and Te. In situ Fourier transform infrared (FTIR) spectroscopy and density functional theory (DFT) calculation in detail explain the essence of the promotion in the C-C bond cleavage and electrochemical performance. This work provides an efficient strategy for the energy conversion in DEFCs.

2. Experimental section

2.1. Synthesis of Pd NSs seeds

To prepare Pd NSs, 10 mg Na_2PdCl_4 , 30 mg $\text{W}(\text{CO})_6$, 40 mg PVP, 5 mL DMF and 1 mL CH_3COOH were added into a reaction flask (30 mL). After ultrasonication for 40 min, the homogeneous mixture was heated from room temperature to 140 °C for 0.5 h and maintained for 1 h in an oil bath. The obtained products were cooled to 80 °C for further use.

2.2. Synthesis of S-Pd NSs, Se-Pd NSs and Te-Pd NSs

In order to synthesize Te-Pd NSs, 0.7 mg H_6TeO_6 , 3.6 mg $\text{C}_6\text{H}_6\text{O}_3$, 50 μL HCOOH and 1 mL DMF were put into a glass bottle. After ultrasonication for around 5 min, the resulting homogeneous mixture was poured into the Pd NSs. Then the mixture was heated from 80 °C to 140 °C in 20 min and maintained at 140 °C for 2 h. The resulting colloidal products were collected by centrifugation and washed with ethanol/acetone mixture. The synthetic conditions for S-Pd NSs and Se-Pd NSs were similar to that of Te-Pd NSs except for changing 0.7 mg H_6TeO_6 with 0.3 mg $\text{CH}_3\text{N}_3\text{S}$ and 0.4 mg H_2SeO_3 , respectively.

2.3. Preparation of S-Pd NSs/C, Se-Pd NSs/C and Te-Pd NSs/C

The as-obtained Pd-based chalcogenide samples were mixed with Vulcan XC-72R carbon and dispersed in a mixture of 1 mL ethanol and 4 mL CHCl_3 . The mixture was sonicated for 30 min. Subsequently, the supported catalysts were collected by centrifugation at 10,000 rpm for 3 min and dried in an oven at 50 °C. 2 mg catalysts were dispersed in 0.5 mL isopropanol and 5 μL Nafion (5 wt%) and sonicated for 30 min to form a uniform ink.

2.4. Characterization

Transmission electron microscopy (TEM) was conducted by JEM 1400 with an acceleration of 100 kV. High-resolution TEM (HRTEM) and high-angle annular dark-field scanning TEM energy-dispersive X-ray spectroscopy (HAADF-SEM-EDS) elemental mapping were obtained on an FEI Tecnai F30 high-resolution transmission electron microscope at an acceleration voltage of 300 kV. The content of samples was determined by the inductively coupled plasma atomic emission spectroscopy (iCap 7400, Thermo Fisher, ICP-OES). Scanning electron microscope EDS (SEM-EDS) was obtained on a scanning electron microscope (ZEISS Sigma SEM)). Powder X-ray diffraction (PXRD) was collected on an X'Pert-Pro mean population doubling diffractometer (Netherlands PANalytical) with a $\text{Cu K}\alpha$ x-ray source ($\lambda = 1.542 \text{ \AA}$). X-ray photoelectron spectroscopy (XPS) analysis was carried out with a Surface Science Instruments S-Probe XPS Spectrometer. The carbon peak at 284.8 eV was used as a reference to correct. Atomic force microscopy (AFM) image was performed on a Bruker Dimension Icon. X-ray

absorption spectroscopy (XAS) data were collected at the ODE beamline of the Soleil Synchrotron (France). Data were processed according to standard procedures using the Demeter program package (Version 0.9.24 52).

2.5. Electrochemical measurement

All the electrochemical measurements were conducted by the CHI 760E electrochemical analyzer (CH Instruments, Chenhua Co, Shanghai, China) in a standard three-electrode system. Glass carbon electrode (GCE, diameter of 5 mm, area: 0.196 cm^2) loaded with catalysts, graphite rod, and saturated calomel electrode (SCE) were employed as a working electrode, counter electrode, and reference electrode, respectively. All potentials were converted to the values in reference to the reversible hydrogen electrode (RHE) by using the formula: $E(\text{vs RHE}) = E(\text{vs SCE}) + 0.0591 \text{ pH} + 0.24 \text{ V}$. 2.5 μL ink was spread to GCE and dried naturally.

Electro-chemical impedance spectroscopy (EIS) was measured using a CHI 760E electrochemical workstation with an AC signal amplitude of 5 mV in the frequency range from 1000 kHz to 0.1 Hz. The electrochemical active surface area (ECSA) was determined by integrating the area of the reduction peak of PdO on the CVs at the rate of 50 mV s^{-1} in 1 M KOH solution. The CV measurements of EOR, EGOR and MOR were scanned in 1 M KOH and 1 M alcohol at the rate of 50 mV s^{-1} . The ECSA ($\text{m}^2 \text{ g}^{-1}$) of catalysts was estimated according to Eq. (1).

$$\text{ECSA} = Q / (0.405 \times W_{\text{Pd}}) \quad (1)$$

where W_{Pd} is Pd loading ($\text{mg} \cdot \text{cm}^{-2}$), determined by the ICP-OES, on the electrode, Q is the Coulombic charge by integrating the peak area of the reduction of PdO (mC), and 0.405 represents the charge required for the reduction of a PdO monolayer ($\text{mC} \cdot \text{cm}^{-2}$).

The chronoamperometry measurements were conducted at $0.6 V_{\text{RHE}}$ in the 1 M KOH + 1 M ethanol solution for 7200 s. For the CO stripping tests, the CO oxidation experiments were carried out in 1 M KOH solution. Before the test, the solution was bubbled with CO gas (99.9%) for 15 min. The ECSA_{CO} can be determined according to Eq. (2) based on CO stripping.

$$\text{ECSA}_{\text{CO}} = Q_{\text{CO}} / (m \times q_{\text{CO}}) \quad (2)$$

where Q_{CO} is the charge used for the oxidation of CO (mC cm^{-2}), m is the loading amount of noble metal, and q_{CO} is the charge required to oxidize the monolayer of CO ($420 \mu\text{C cm}^{-2}$) on the catalyst.

The Faradaic efficiency is calculated at $0.6 \sim 0.9 V_{\text{RHE}}$ for 7200 s in the 1 M KOH + 1 M ethanol solution as the Eqs. (3) and (4):

$$\text{FE}_{\text{C2}} = m_{\text{C2}} \times 4 \times F / Q_{\text{total}} \quad (3)$$

$$\text{FE}_{\text{C1}} = 1 - \text{FE}_{\text{C2}} \quad (4)$$

where FE_{C2} and FE_{C1} represent the Faradaic efficiency of EOR C2 pathway and C1 pathway, respectively. m_{C2} is the mole number of C2 products. F is the Faraday constant equal to $96,500 \text{ C/mol}$. 4 comes from the 4-electron transferring in the EOR C2 pathway. Q_{total} is the integration of the current signals versus time, i.e. $Q_{\text{total}} = \int_0^t I(t) dt$.

In situ FTIR measurements were conducted using a Nexus 870 spectrometer (Nicolet) equipped with a liquid nitrogen-cooled MCT-A detector. The homemade electrochemical cell consists of a CaF_2 window and a thin layer ($\leq 10 \mu\text{m}$) between the GCE and CaF_2 window. The three-electrode system was used to finish the electrochemical measurements. FTIR measurements were recorded from 0.3 to $1.3 V_{\text{RHE}}$ with an interval of 0.1 V for Pd NSs and Te-Pd NSs. The resulting spectra were obtained and calculated as the relative change in reflectivity based on Eq. (5).

$$\Delta R/R = [R(E_s) - R(E_R)] / R(E_R) \quad (5)$$

where $R(E_s)$ and $R(E_R)$ are the single-beam spectra collected at the

catalyst's potential E_s and reference potential E_R , respectively.

η was calculated to evaluate the selectivity for ethanol oxidation to CO_3^{2-} according to Eq. (6):

$$\eta = [(\text{CO}_3^{2-})/2] / [(\text{CH}_3\text{COO}^-) + (\text{CO}_3^{2-})/2] \quad (6)$$

2.6. Computational details

All calculations in this work were performed by the density functional theory (DFT) within the Vienna ab initio simulation package (VASP). In all calculations, the generalized gradient approximation (GGA) with the Perdew–Burke–Ernzerhof (PBE) function was selected. The cut-off energy was set to 400 eV for plane wave expansion and a Monkhorst–pack mesh of $3 \times 3 \times 1$ k-points was used to sample the Brillouin zone. For the geometry optimizations, the convergence criteria of the force and energy were set to $0.03 \text{ eV } \text{\AA}^{-1}$ and 10^{-5} eV , respectively. The vacuum space was more than 18 \AA , large enough to avoid interplanar interactions. For pure Pd catalyst, a $p(3 \times 3)$ three-atomic-layer slab was applied to model the Pd (111) surface. To simulate the effects of Te dopants, the third layer of Pd (111) was replaced with one Te atom.

The adsorption energies were calculated by $\Delta E_{\text{ads}} = E_{\text{ads}+\text{sur}} - (E_{\text{ads}} + E_{\text{sur}})$, where $E_{\text{ads}+\text{sur}}$ represents the total energy of the adsorbate

interacting with the surface, E_{ads} is the energy of the adsorbate, and E_{sur} is the energy of the bare surface. The free energy change (ΔG) of each elementary reaction was calculated according to Eq. (7):

$$\Delta G = \Delta E + \Delta \text{ZPE} - T\Delta S \quad (7)$$

where ΔE , ΔZPE , and ΔS are the difference of total energy, zero-point energy, and entropy, respectively. T is the temperature (set as 298.15 K).

3. Results and discussion

3.1. Characterization of Pd NSs and NM-Pd NSs

The transmission electron microscopy (TEM) image displays that the Te-Pd NSs (Fig. 1a, the inset is a model diagram of Te-Pd NSs) and Pd NSs (Fig. S1a) are ultra-thin and porous. S-Pd NSs (Fig. S1b) and Se-Pd NSs (Fig. S1c) also present similar nanoflake morphologies. High-resolution TEM (HRTEM) image of Te-Pd NSs shows a lattice spacing of 0.23 nm in coincidence with Pd (111) facet, identical to the Pd NSs, S-Pd NSs and Se-Pd NSs (Fig. 1b and Fig. S2). The elemental distributions of Pd and Te in Te-Pd NSs were characterized by high-angle annular dark-field scanning TEM energy-dispersive X-ray spectroscopy (HAADF-STEM-EDS) elemental mapping (Fig. 1c). The Pd signals (orange) mainly concentrate on the nanosheet while Te signals (green) evenly distribute, implying small amounts of Te in Te-Pd NSs [33–36]. Furthermore,

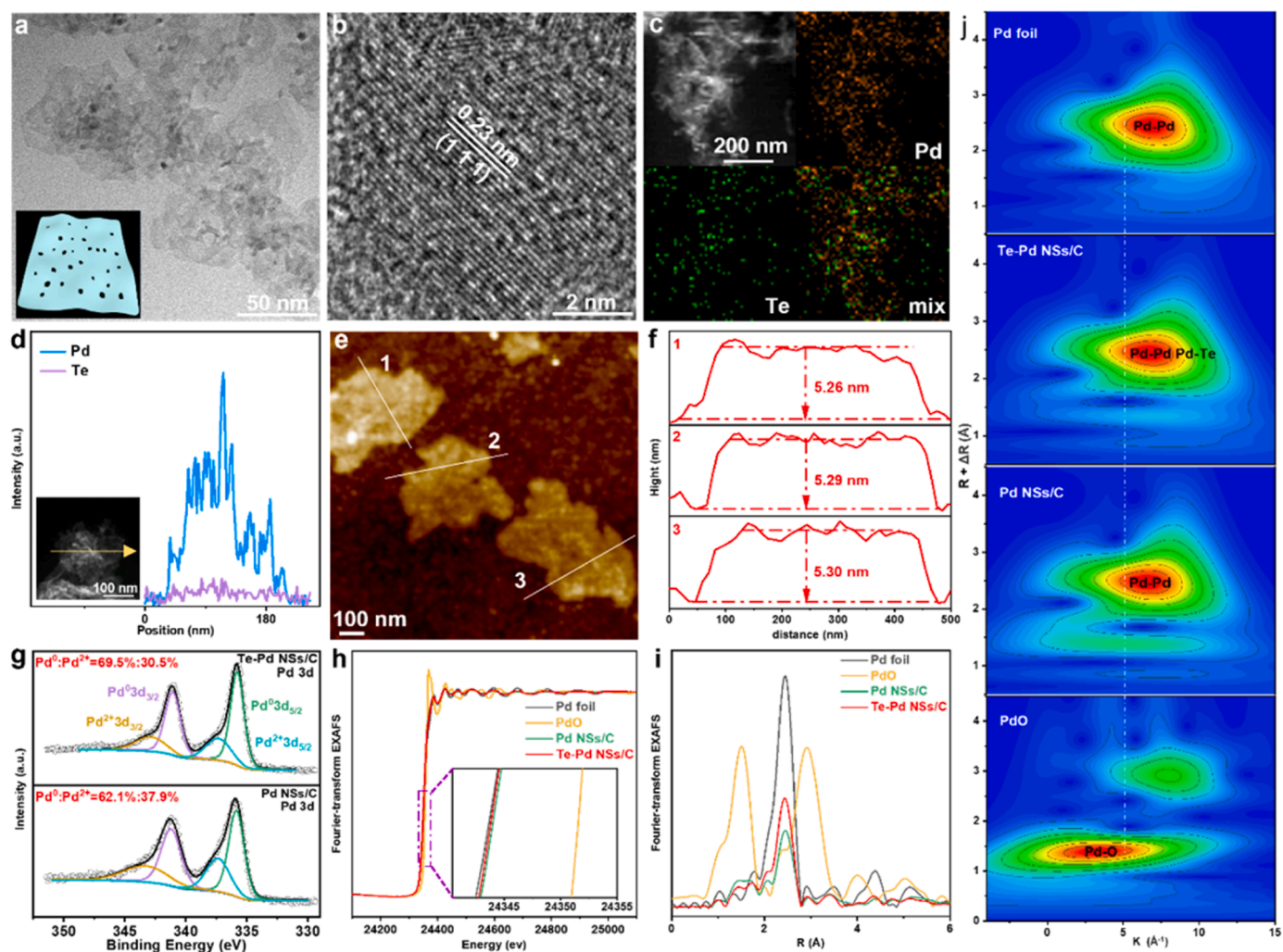


Fig. 1. (a) TEM image, (b) HRTEM image and (c) HAADF-STEM-EDS elemental mapping of Te-Pd NSs. (d) Line-scanning results of Pd and Te in Te-Pd NSs. (e) AFM image and (f) corresponding height profiles of Te-Pd NSs. (g) Pd 3d XPS spectra of Te-Pd NSs/C and Pd NSs/C. (h) Pd K-edge XANES spectra, (i) Fourier-transform EXAFS and (j) wavelet transform for EXAFS spectra of Pd foil, Pd NSs/C, Te-Pd NSs/C and PdO.

line-scanning results also indicate that the content of Pd is prominently higher than Te (Fig. 1d). The scanning electron microscope-energy dispersive X-ray spectroscopy (SEM-EDS) test was conducted to determine the molar amount -

of chalcogenide added. The chalcogenide content is about 12.0% from EDS in Fig. S3. The average thickness of Te-Pd NSs is about 5.28 nm, as determined by atomic force microscopy (AFM) (Fig. 1e and f). The nanocrystal phase was studied by the powder X-ray diffraction (PXRD) pattern in Fig. S4. The diffraction peaks of Te-Pd NSs, S-Pd NSs and Se-Pd NSs are in line with Pd NSs (JCPDS no.87-0643), suggesting that the crystal structure of pristine Pd NSs is slightly influenced by low and superficial Te, S and Se doping [36]. To evaluate electrocatalytic performances, the as-prepared Palladium chalcogenide nanosheets were further loaded on Vulcan XC-72R carbon. All subsequent characterization and evaluation are based on supported catalysts unless otherwise stated [37,38]. Prior to the electrochemical evaluation, TEM, EDS and PXRD of samples before and after loading were compared to understand the loading effect on the physical properties of nanosheets. Although it is difficult to characterize the nanosheet thickness after loading, there is no obvious aggregation found, indicating that the morphology of nanosheets is maintained during the loading (Figs. 1a, S1 and S5).

Furthermore, the content ratios of Pd to chalcogenide in EDS are consistent before and after loading (Fig.S3 and S6). PXRD of Pd NSs/C and NM-Pd NSs/C also shows that the nanocrystal phases are the same as that before loading (Fig. S4 and S7). Thus, the loading on Vulcan XC-72R carbon black does not affect the morphology, component ratio and nanocrystal phase of the samples. ICP-OES results of the as-obtained supported palladium chalcogenide nanosheets were given in Table S1.

XPS results of Te-Pd NSs/C show that the two peaks for the Pd 3d_{5/2} and Pd 3d_{3/2} states can be split into two doublets, associated with Pd⁰ and Pd²⁺, respectively. The ratio of Pd⁰ to Pd²⁺ on Te-Pd NSs/C (Fig. 1g) is higher than that of Pd NSs/C followed by S-Pd NSs/C and Se-Pd NSs/C (Fig. S8). An increase in the proportion of Pd⁰ implies the presence of more Pd active sites [36]. Two doublets for Te 3d_{5/2} and Te 3d_{3/2} can be deconvoluted into two peaks assigned to Te⁰ and oxidized Te⁴⁺, respectively (Fig. S9). The presence of Te⁴⁺ is derived from the inevitable air oxidation while Te⁰ might come from the interaction with palladium metal [6,39]. Thus, the introduction of Te into the Pd NSs leads to more Pd⁰ active sites via the mutual effect between Pd and Te. This will be further demonstrated below.

To further evaluate the local microenvironment and chemical bond information on the Te-Pd NSs, we characterized electrocatalysts with the

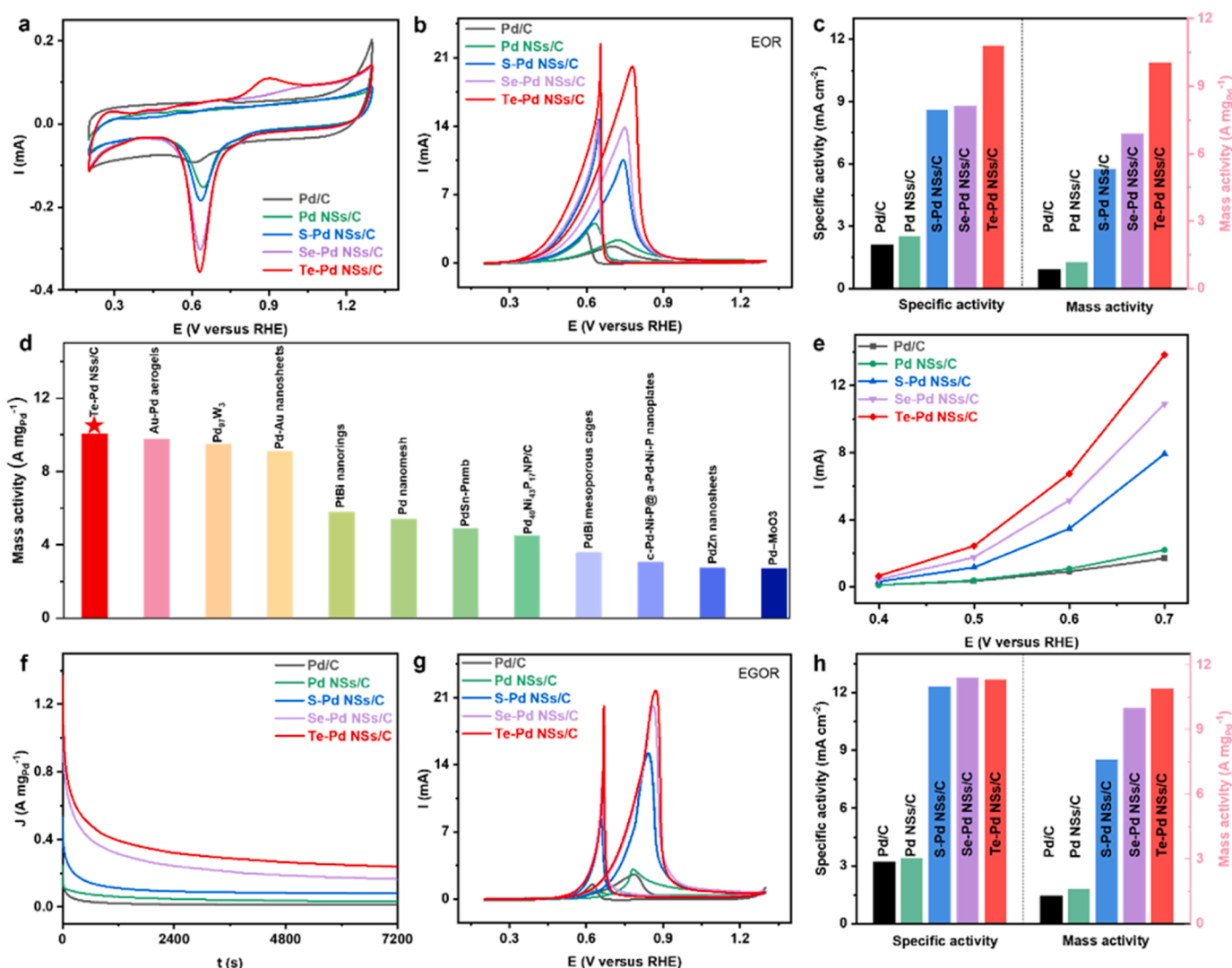


Fig. 2. Cyclic voltammogram curves (a) in 1 M KOH and (b) in 1 M KOH + 1 M ethanol solution of catalysts. (c) Comparison of catalytic performances. (d) Comparison between Te-Pd NSs/C and other reported EOR catalysts. (e) Current intensity at the indicated potentials and (f) i-t curves (at 0.6 V_{RHE}) of catalysts towards EOR in a 1 M KOH+ 1 M ethanol solution. (g) Cyclic voltammogram curves and (h) comparison of catalytic performance of catalysts towards EGOR in a 1 M KOH+ 1 M EG solution.

XAS technique. As revealed by the Pd K-edge from X-ray absorption near-edge structures (XANES) in Fig. 1h and the insert, the absorption edge of Te-Pd NSs/C is located at a lower energy position than Pd NSs/C, suggesting the content of metallic Pd in Te-Pd NSs is higher than Pd NSs [39,40], which is consistent with the XPS results. Fig. 1i shows the Pd extended X-ray absorption fine structure (EXAFS) spectra. The Pd-Pd bond on Te-Pd NSs/C at 2.40 Å keeps pace with that of Pd foil, indicating that metallic Pd dominates in these two catalysts. Since Te-Pd NSs/C presents a higher peak signal at 2.40 Å compared to Pd NSs/C and Te exists as a surface-doped atom on the Te-Pd NSs/C as mentioned above, Pd⁰ and Te⁰ interact to form Pd-Te bond in Te-Pd NSs. EXAFS wavelet transform (Fig. 1j) confirms that Pd foil has a maximum contour intensity at 8.47 Å⁻¹ assigned to Pd-Pd. The region with the maximum intensity on Te-Pd NSs/C is closer to Pd foil and away from PdO compared with Pd NSs/C due to the effect of Pd and Te interaction [41, 42]. It is further proved that Pd atom is coordinated with the Te atom and the introduction of Te contributes to the formation of more Pd⁰ active sites in Te-Pd NSs/C.

3.2. Electrocatalytic EOR, EGOR and MOR processes

The typical cyclic voltammetry (CV) curves over different catalysts were obtained in 1 M KOH solution at a scan rate of 50 mV s⁻¹ (Fig. 2a). A reduction peak at about 0.63 V_{RHE} is attributed to the transformation of Pd-O into Pd. By comparison, the Te-Pd NSs/C shows the most remarkable reduction peak among these catalysts. Commercial Pd/C and NM-Pd NSs/C catalysts were evaluated in EOR, EGOR and MOR in alkaline media. For comparison, the mass activity and the specific activity (Fig. 2c) were calculated by normalizing current (Fig. 2b) to the Pd mass loaded and electrochemical surface area (ECSA, in Supporting Information), respectively. The ECSAs of commercial Pd/C, Pd NSs/C and NM-Pd NSs/C are in Table S2. For EOR, S-Pd NSs/C, Se-Pd NSs/C and Te-Pd NSs/C show preeminent mass activity and specific activity compared with Pd/C and Pd NSs/C. Among them, the Te-Pd NSs/C presents the highest mass activity of 10.0 A mg⁻¹ Pd and excellent specific activity of 11.7 mA cm⁻² toward EOR. They are 6.6 (4.1), 8.6 (4.2), 12.5 (5.6) times higher mass activity (specific activity) than commercial Pd/C (Fig. 2c), respectively, and 4.4 (3.4), 5.8 (3.5), 8.3 (4.7)-fold higher mass activity (specific activity) than Pd NSs/C simultaneously. Te-Pd NSs/C has exhibited the highest mass activity, far exceeding the Pd-based catalysts already reported in the literature (Fig. 2d and Table S3). With the increase of potential, a significant rise of the current intensity further indicates the high reaction rate on NM-Pd NSs/C, especially Te-Pd NSs/C (Fig. 2e).

The chronoamperometry (CA) measurement tests were conducted to test the durability of catalysts. NM-Pd NSs/C remains higher significant mass activity during the test than Pd/C and Pd NSs/C, which decay rapidly (Fig. 2f), suggesting a superior long-term mass activity for EOR. After the CA measurement tests, NM-Pd NSs/C and Pd NSs/C present slight agglomeration in Fig. S10. The chalcogenide content in the electrocatalysts (in Fig. S11) loses to some extent in comparison with the fresh samples Fig. S6. For EGOR and MOR, supported palladium chalcogenide nanosheets demonstrate the long-term higher activity than Pd/C and Pd NSs/C in Fig. S12. Additionally, Te-Pd NSs/C (Fig. S13) after 1000 cycles of CV exhibits the least decay of electrochemical activity among the catalysts followed by Se-Pd NSs/C and S-Pd NSs/C, which are smaller than that of Pd/C and Pd NSs/C, indicating that Te-Pd NSs/C, Se-Pd NSs/C and S-Pd NSs/C catalysts are more stable than Pd/C and Pd NSs/C. As shown in Fig. 2g, h and Table S4, NM-Pd NSs/C also exhibits relatively high mass and specific activity for the EGOR. They are 5.8 (3.8), 7.7 (4.0) and 8.4 (4.0)-fold higher mass activity (specific activity) than commercial Pd/C, respectively and 4.8 (3.6), 6.3 (3.8) and 6.8 (3.7) times higher mass activity (specific activity) than Pd NSs/C, respectively. As we expected, these three catalysts also demonstrate excellent activity in MOR. They present 3.6 (2.4), 6.3 (3.2) and 9.9 (4.7) times higher mass activity (specific activity) than commercial Pd/C and 2.2

(1.7), 3.7 (2.2) and 5.9 (3.2) times higher than Pd NSs/C, respectively (Fig. S14 and Table S5). Thus, the Te-Pd NSs/C demonstrates the highest mass activity and specific activity among all these catalysts for EOR, EGOR and MOR. The toxicity resistance of electrocatalysts to carbonaceous intermediates was investigated by CO stripping experiments. The potential of CO oxidation over Te-Pd NSs/C is 0.769 V_{RHE}, which exhibits a significant negative shift compared with Pd/C at 0.806 V_{RHE} and Pd NSs/C at 0.802 V_{RHE} (Fig. S15). Additionally, the potentials over S-Pd NSs/C and Se-Pd NSs/C are also lower than commercial Pd/C and Pd NSs/C. Te-Pd NSs/C has the most robust CO oxidation capacity among all the NM-Pd NSs/C, indicating high resistance to carbon monoxide intermediate poisoning. The introduction of chalcogenides improves the oxidation of carbon monoxide intermediates to enhance the resistance ability of the NM-Pd NSs/C to CO poisoning. Furthermore, CO stripping experiment was used to determine the ECSAs of all catalysts (ECSA_{CO}). Both ECSA_{CO} (in Supporting Information) and ECSAs increase with the doping of chalcogenides though ECSA_{CO} is slightly larger than ECSAs (Table S2). To understand the electron transfer resistance in the electrochemical reaction, we conducted EIS analysis at 0.6 V_{RHE} (Fig. S16). The EIS of catalysts is based on a model with one time constant, where includes the solution resistance (R_s) and charge transfer resistance (R_{ct}). Te-Pd NSs/C presents the lowest R_{ct} value (77.62 Ω) among all the electrocatalysts. Meanwhile, the R_{ct} values of S-Pd NSs/C (172.1 Ω) and Se-Pd NSs/C (84.3 Ω) also are lower than Pd NSs/C (288.2 Ω) and commercial Pd/C (362.8 Ω). S-Pd NSs/C and Se-Pd NSs/C, especially Te-Pd NSs/C have by far the lower electron transferring resistance than Pd NSs/C and commercial Pd/C. This partially accounts for higher EOR performance of NM-Pd NSs/C than Pd NSs/C and commercial Pd/C.

3.3. Reaction mechanism

In order to further explore the reaction mechanism and reaction pathway for EOR, the in situ FTIR spectra of EOR on Pd NSs/C and Te-Pd NSs/C were analyzed at different potentials from 0.3 to 1.3 V_{RHE} with an interval of 0.1 V in Fig. 3a and b. The vibration peaks at 1053 and 1098 cm⁻¹ are attributed to the stretching vibration of the C-O bond on ethanol [43,44]. On these two catalysts, consumed ethanol increases with the increase of potentials during the oxidation reaction. The other three vibration peaks at about 1348, 1413 and 1551 cm⁻¹, respectively, are attributed to the bending vibration of -CH₃ in adsorbed CH₃COO⁻, the symmetric and asymmetric stretching bond of O-C-O in CH₃COO⁻ [2, 21,26,28,45–47].

The ethanol oxidation on Te-Pd NSs/C occurs at a lower potential (0.6 V_{RHE}) than that on Pd NSs/C (0.7 V_{RHE}) (Fig. S17), implying the reduced energy barrier for EOR on Te-Pd NSs/C. In addition, we found that CO₃²⁻ at 1406 cm⁻¹ (Compared to the theoretical value of 1390 cm⁻¹, there is a positive displacement due to the influence of the electrolyte) is overlapped with CH₃COO⁻ at 1413 cm⁻¹ (Fig. 3c) [44]. As shown in Fig. 3c, the intensity of the infrared absorption band at about 1413 cm⁻¹ on Te-Pd NSs/C is significantly higher than that of the infrared absorption band at 1551 cm⁻¹, which is different from the spectrum of standard CH₃COO⁻ (spectrum B). The contribution of CH₃COO⁻ (spectrum B) to the in-situ spectrum (spectrum A) can be excluded by the subtraction method. As a result, spectrum C (i.e., C = A - 1.46 * B) is obtained. The C-O vibration strength of carbonate can be determined compared to spectrum D of 0.1 M Na₂CO₃ solution. Similarly, carbonate for ethanol oxidation on commercial Pd/C is also identified at 0.8 V_{RHE} (Fig. S18). By subtraction, we separate the CO₃²⁻ signal from the sum of CH₃COO⁻ and CO₃²⁻, proving the presence of the CO₃²⁻ on Te-Pd NSs/C, Pd NSs/C and Pd/C in the electrochemical reaction [44,48].

The selectivity of C1 pathway, η, was illustrated in Fig. 3d. We found that the η on Te-Pd NSs/C (0.177) is by far the higher than that of Pd NSs/C (0.120) and commercial Pd/C (0.072), indicating that Te-Pd NSs/C is more conducive to the cleavage of C-C bond than Pd NSs/C and commercial Pd/C. In addition, the products were analyzed by ¹H NMR to

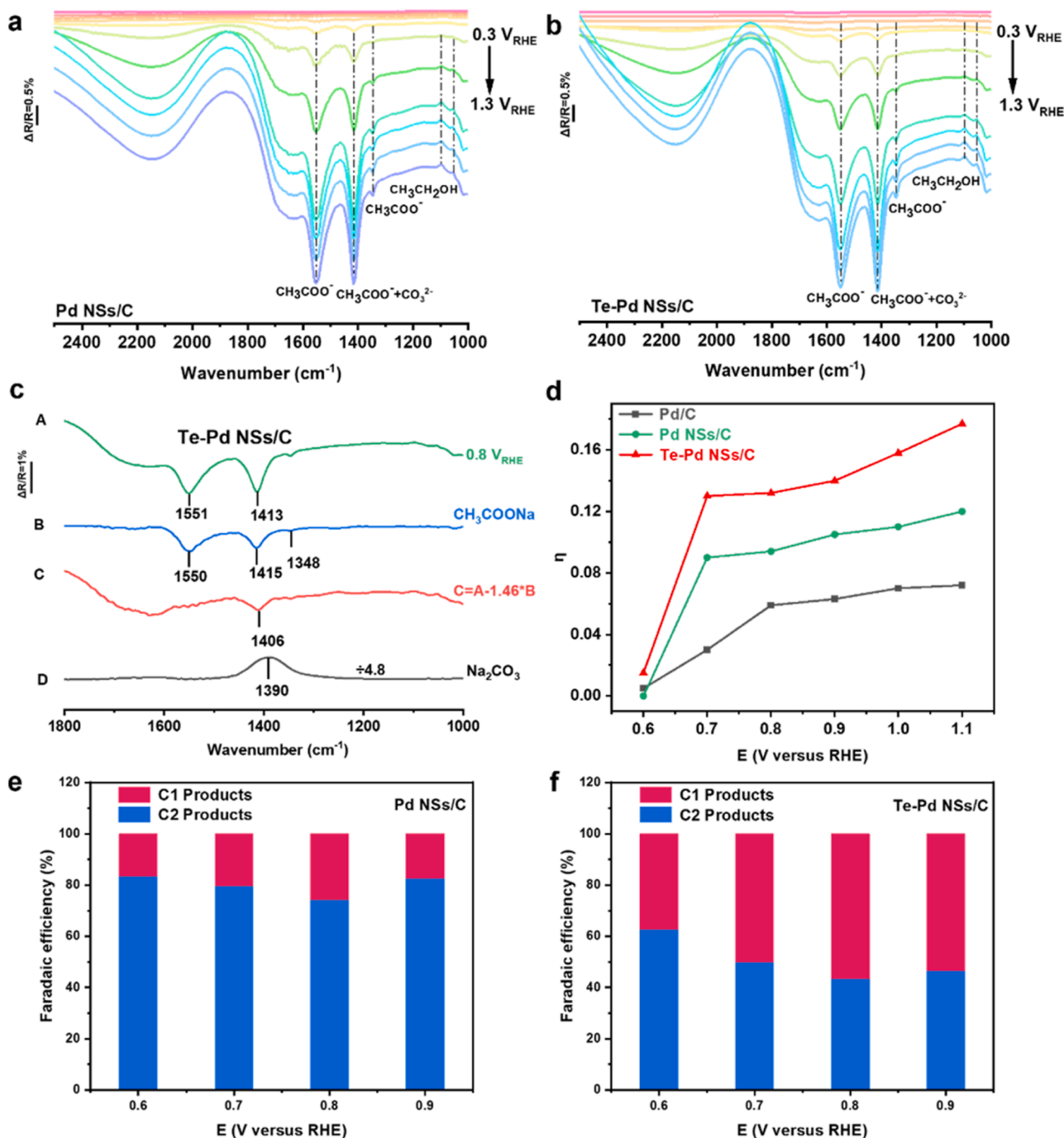


Fig. 3. Electrochemical in situ FTIR spectra of (a) Pd NSs/C and (b) Te-Pd NSs/C in 1 M KOH + 1 M ethanol solution. (c) Identification of carbonate as products of ethanol oxidation on Te-Pd NSs/C at 0.8 V_{RHE} . (d) The selectivity (η) for complete ethanol oxidation to CO_3^{2-} from 0.6 to 1.1 V_{RHE} . The Faradaic efficiency of C1 pathway and C2 pathway from 0.6 to 0.9 V_{RHE} of (e) Pd NSs/C and (f) Te-Pd NSs/C.

evaluate the cleavage ability of C-C bond on the catalysts after CA test from 0.6 to 0.9 V_{RHE} . The FE of C1 pathway for Te-Pd NSs/C (56.6%) is higher than that for Pd NSs/C (25.7%) at 0.8 V_{RHE} for EOR in Fig. 3e and f, indicating that the introduction of Te can significantly improve the ability of Pd NSs to break C-C bond.

In order to further elucidate the reasons for the improvement of the mass activity and selectivity of C1 pathway on Te-Pd NSs/C in the EOR reaction, DFT calculations were conducted. From the partial density of states (PDOS) in Fig. 4a, we found that the energy of the Pd 4d orbital matches well with the Te 4p, proving that there exists a p-d hybridization between Pd and Te [7,49]. The p-d hybridization leads to the rearrangement of the electronic structure on Pd. In Fig. 4b, the d-band

center of Te-Pd NSs ($\epsilon_d = -1.754$ eV) shifts down compared to Pd NSs ($\epsilon_d = -1.649$ eV), which indicates that the adsorption of intermediate species is weakened on Te-Pd NSs, facilitating the removal of the intermediate and enhancing the ability of toxicity resistance [49]. The free energy of ethanol oxidation is shown in Fig. 4c. The atomic structure models of the corresponding reaction intermediates are presented for Te-Pd NSs and Pd NSs in Fig. 4d and Fig. S19. Ethanol is converted through dehydrogenation, cleavage process and further oxidation to carbon dioxide. Among them, the step from $^*\text{CH}_3\text{CO}$ to $^*\text{CH}_3\text{COOH}$ is regarded as a rate-determining one in view of the relatively high reaction energy barrier. For $^*\text{CH}_3\text{COOH}$ production, Te-Pd NSs (0.706 eV) exhibit a higher reaction energy barrier than Pd NSs (0.565 eV),

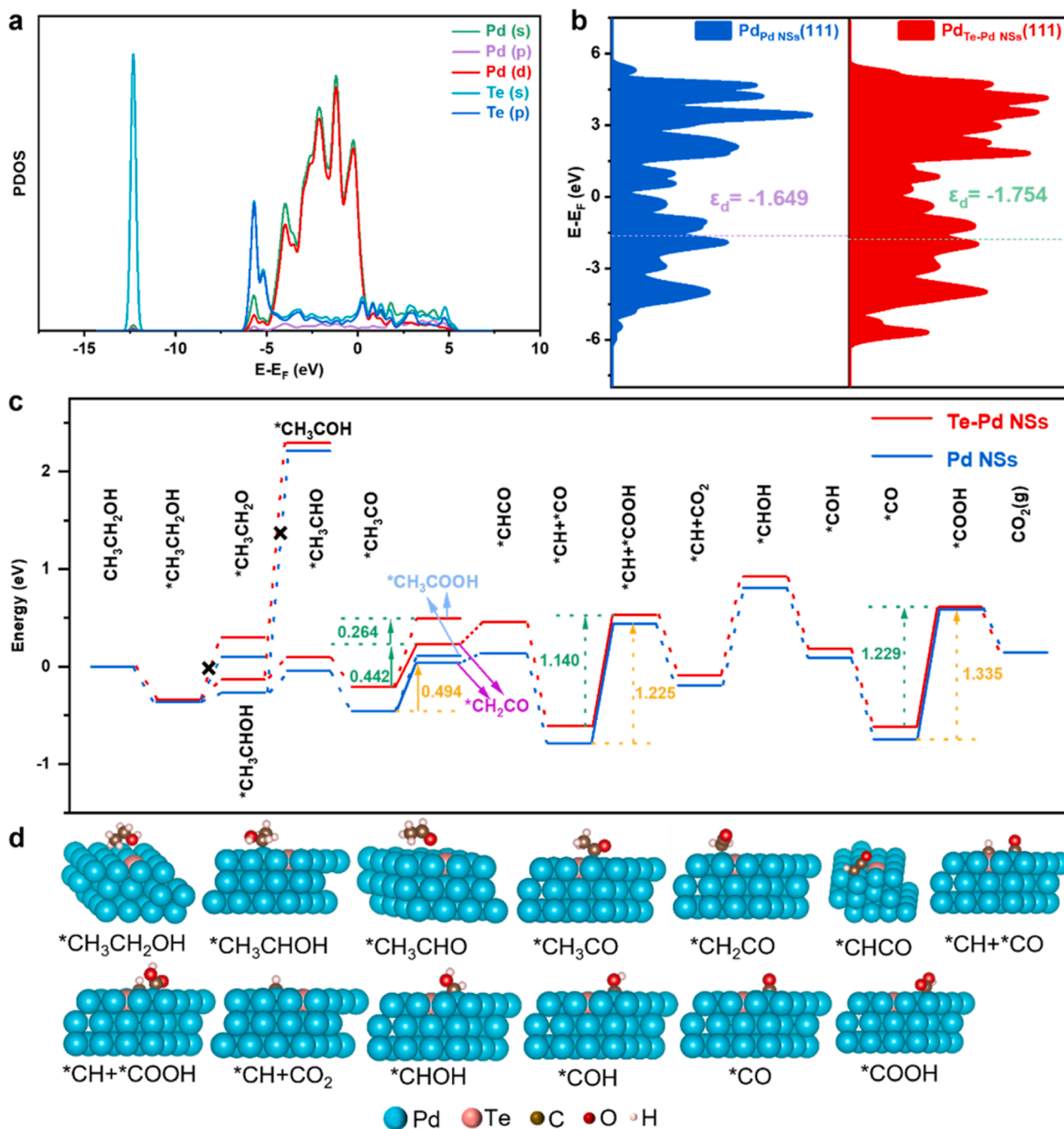


Fig. 4. (a) The PDOS and (b) PDOS of d-bands of the surfaces of Pd_{Pd} NSs (111) and Pd_{Te-Pd} NSs (111). (c) The calculated free energy diagram of ethanol electrooxidation reaction on the Pd NSs surface and Te-Pd NSs surface. (d) The structures of reaction intermediates during ethanol electrooxidation on the Pd (111) surface of Te-Pd NSs.

implying that the C2 pathway occurs rarely on Te-Pd NSs. More importantly, the reaction from *CH₃CO to CO₂ via *CH₂CO presents a lower energy barrier on Te-Pd NSs (0.442 eV) than Pd NSs (0.494 eV), indicating the C1 path dictates ethanol electrochemical oxidation. In this reaction pathway, the steps from *CH and *CO to *CH and *COOH and from *CO to *COOH are the rate-determining steps because of the similar energy barriers [50,51]. Strikingly, Te-Pd NSs have a lower reaction energy barrier than Pd NSs in these two steps. Therefore, CO₂ on Te-Pd NSs is more likely generated than on Pd NSs. This also explains why Te-Pd NSs have higher C1 pathway selectivity and superior mass activity than Pd NSs.

4. Conclusion

To summarize, benefiting from p-d hybridization via the interaction between chalcogenides and Pd, chalcogenide surface-doped Pd NSs/C shows extraordinary EOR, EGOR and MOR mass activity and outstanding C1 pathway selectivity. At the same time, it also shows high anti-carbon monoxide poisoning performance and long-lasting stability under alkaline conditions. The mass activity of chalcogenides surface-doped Pd NSs/C outperforms not only commercial Pd/C and Pd NSs/C, but also most of the Pd-based catalysts reported for EOR, EGOR and MOR under alkaline conditions. In situ. FTIR studies and ¹H NMR reveal that the selectivity and FE of the C1 pathway are greatly improved on

Te-Pd NSs/C compared to Pd NSs/C for EOR. Characterization results show that the introduction of S, Se and Te adjusts the adsorption energy of intermediates, promoting the oxidation of carbon monoxide and increasing the intrinsic activity of the catalysts. DFT results show that the reaction energy barrier on Te-Pd NSs significantly decreases in the rate-determining steps compared with Pd NSs, thereby improving the C1 pathway selectivity and electrochemical activity. This paper directs the preparation of high-activity catalysts for EOR, EGOR and MOR and provides a deeper understanding of the selective alcohol electro-oxidation on Pd-based electrocatalysts.

CRedit authorship contribution statement

Liping Wang: Data curation, Methodology, Investigation, Writing – review & editing. **Zhiyong Yu:** Data curation, Methodology. **Wei Yan:** Data curation, Methodology. **Liangbin Liu:** Data curation, Methodology. **Mengjun Wang:** Methodology. **Qingyu Kong:** Data curation. **Zhiwei Hu:** Data curation. **Hongbo Geng:** Data curation. **Xiaoqing Huang:** Project administration, Methodology, review & editing. **Yunhua Li:** Project administration, Calculation, Writing - review & editing.

Declaration of Competing Interest

The authors declare that they have no known competing financial interests or personal relationships that could have appeared to influence the work reported in this paper.

Data Availability

Data will be made available on request.

Acknowledgments

This work was supported by the National Natural Science Foundation of China (Grant No.220728270, 22025108, U21A20327). S. Fang and T. Wu from Information and Network Center of Xiamen University are acknowledged for the help with the GPU computing. Y. Yu, S. Fang and Z. Xu from Information and Network Center of Xiamen University are acknowledged for the help with the high-performance computing. We acknowledge support from the Max Planck-POSTECH-Hsinchu Center for Complex Phase Materials.

Appendix A. Supporting information

Supplementary data associated with this article can be found in the online version at [doi:10.1016/j.apcatb.2023.123564](https://doi.org/10.1016/j.apcatb.2023.123564).

References

- [1] X. Fu, C. Wan, Y. Huang, X. Duan, Noble metal based electrocatalysts for alcohol oxidation reactions in alkaline media, *Adv. Funct. Mater.* 32 (2022), 2106401, <https://doi.org/10.1002/adfm.202106401>.
- [2] E. Monyoncho, S. Steinmann, C. Michel, E. Baranova, T. Woo, P. Sautet, Ethanol electro-oxidation on palladium revisited using polarization modulation infrared reflection Absorption Spectroscopy (PM-IRRAS) and Density Functional Theory (DFT): why is it difficult to break the C–C Bond? *ACS Catal.* 6 (2016) 4894–4906, <https://doi.org/10.1021/acscatal.6b00289>.
- [3] M.Z.F. Kamarudin, S.K. Kamarudin, M.S. Masdar, W.R.W. Daud, Review: direct ethanol fuel cells, *Int. J. Hydrog. Energy* 38 (2013) 9438–9453, <https://doi.org/10.1016/j.ijhydene.2012.07.059>.
- [4] H. Wang, Z. Liu, Comprehensive mechanism and structure-sensitivity of ethanol oxidation on platinum: new transition-state searching method for resolving the complex reaction network, *J. Am. Chem. Soc.* 130 (2008) 10996–11004, <https://doi.org/10.1021/ja801648h>.
- [5] A. Vilaplana, C. Rogero, J. Feliu, E. Herrero, Cleavage of the C–C bond in the ethanol oxidation reaction on platinum: insight from experiments and calculations, *J. Phys. Chem. C* 120 (2016) 11590–11597, <https://doi.org/10.1021/acs.jpcc.6b03117>.
- [6] Q. Zhang, K. Wang, M. Zhang, T. Chen, L. Li, S. Shi, R. Jiang, Electronic structure optimization boosts Pd nanocrystals for ethanol electrooxidation realized by Te doping, *CrystEngComm* 24 (2022) 5580–5587, <https://doi.org/10.1039/d2ce00710j>.
- [7] Y. Qin, W. Zhang, F. Wang, J. Li, J. Ye, X. Sheng, C. Li, X. Liang, P. Liu, X. Wang, X. Zheng, Y. Ren, C. Xu, Z. Zhang, Extraordinary p–d hybridization interaction in heterostructural Pd–PdSe nanosheets boosts C–C bond cleavage of ethylene glycol electrooxidation, *Angew. Chem. Int. Ed.* 61 (2022), e202200899, <https://doi.org/10.1002/anie.202200899>.
- [8] E. Moges, C. Chang, H. Huang, K. Lakshmanan, Y. Awoke, C. Pao, M. Tsai, W. Su, B. Hwang, Sustainable synthesis of dual single-atom catalyst of Pd–N4/Cu–N4 for partial oxidation of ethylene glycol, *Adv. Funct. Mater.* 32 (2022), 2206887, <https://doi.org/10.1002/adfm.202206887>.
- [9] J. Wang, B. Zhang, W. Guo, L. Wang, J. Chen, H. Pan, W. Sun, Toward electrocatalytic methanol oxidation reaction: longstanding debates and emerging catalysts, *Adv. Mater.* 35 (2023), 2211099, <https://doi.org/10.1002/adma.202211099>.
- [10] H. Xu, H. Shang, C. Wang, Y. Du, Recent progress of ultrathin 2D Pd-based nanomaterials for fuel cell electrocatalysis, *Small* 17 (2021), e2005092, <https://doi.org/10.1002/sml.202005092>.
- [11] Z. Yu, S. Xu, Y. Feng, C. Yang, Q. Yao, Q. Shao, Y.F. Li, X. Huang, Phase-controlled synthesis of Pd–Se nanocrystals for phase-dependent oxygen reduction catalysis, *Nano Lett.* 21 (2021) 3805–3812, <https://doi.org/10.1021/acs.nanolett.1c00147>.
- [12] M. Zhou, J. Guo, B. Zhao, C. Li, L. Zhang, J. Fang, Improvement of oxygen reduction performance in alkaline media by tuning phase structure of Pd–Bi nanocatalysts, *J. Am. Chem. Soc.* 143 (2021) 15891–15897, <https://doi.org/10.1021/jacs.1c08644>.
- [13] T. Wang, F. Li, H. Huang, S. Yin, P. Chen, P. Jin, Y. Chen, Porous Pd–PdO nanotubes for methanol electrooxidation, *Adv. Funct. Mater.* 30 (2020), 2000534, <https://doi.org/10.1002/adfm.202000534>.
- [14] A. Chen, C. Ostrom, Palladium-based nanomaterials: synthesis and electrochemical applications, *Chem. Rev.* 115 (2015) 11999–12044, <https://doi.org/10.1021/acs.chemrev.5b00324>.
- [15] L. Yang, X. Wang, D. Liu, G. Cui, B. Dou, J. Wang, Efficient anchoring of nanoscale Pd on three-dimensional carbon hybrid as highly active and stable catalyst for electro-oxidation of formic acid, *Appl. Catal. B Environ.* 263 (2020), 118304, <https://doi.org/10.1016/j.apcatb.2019.118304>.
- [16] T. Song, F. Gao, L. Jin, Y. Zhang, C. Wang, S. Li, C. Chen, Y. Du, From bimetallic PdCu nanowires to ternary PdCu–SnO₂ nanowires: Interface control for efficient ethanol electrooxidation, *J. Colloid Interf. Sci.* 560 (2020) 802–810, <https://doi.org/10.1016/j.jcis.2019.11.009>.
- [17] F. Gao, Y. Zhang, P. Song, J. Wang, C. Wang, J. Guo, Y. Du, Self-template construction of Sub-24 nm Pd Ag hollow nanodendrites as highly efficient electrocatalysts for ethylene glycol oxidation, *J. Power Sources* 418 (2019) 186–192, <https://doi.org/10.1016/j.jpowsour.2019.02.031>.
- [18] Y. Xu, K. Ren, T. Ren, M. Wang, S. Yu, Z. Wang, X. Li, L. Wang, H. Wang, Phosphorus-triggered modification of the electronic structure and surface properties of Pd₄S nanowires for robust hydrogen evolution electrocatalysis, *J. Mater. Chem. A* 8 (2020) 19873–19878, <https://doi.org/10.1039/d0ta07403a>.
- [19] H. Wang, Y. Li, K. Deng, C. Li, H. Xue, Z. Wang, X. Li, Y. Xu, L. Wang, Trimetallic PtPdNi-truncated octahedral nanocages with a well-defined mesoporous surface for enhanced oxygen reduction electrocatalysis, *ACS Appl. Mater. Interfaces* 11 (2019) 4252–4257, <https://doi.org/10.1021/acsami.8b18696>.
- [20] X. Huang, S. Tang, X. Mu, Y. Dai, G. Chen, Z. Zhou, F. Ruan, Z. Yang, N. Zheng, Freestanding palladium nanosheets with plasmonic and catalytic properties, *Nat. Nanotechnol.* 6 (2011) 28–32, <https://doi.org/10.1038/nnano.2010.235>.
- [21] X. Zhou, Y. Ma, Y. Ge, S. Zhu, Y. Cui, B. Chen, L. Liao, Q. Yun, Z. He, H. Long, L. Li, B. Huang, Q. Luo, L. Zhai, X. Wang, L. Bai, G. Wang, Z. Guan, Y. Chen, C.S. Lee, J. Wang, C. Ling, M. Shao, Z. Fan, H. Zhang, Preparation of Au/Pd core-shell nanorods with fcc-2H-fcc heterophase for highly efficient electrocatalytic alcohol oxidation, *J. Am. Chem. Soc.* 144 (2022) 547–555, <https://doi.org/10.1021/jacs.1c11313>.
- [22] G. Yang, Y. Wang, L. Xu, Y. Li, L. Li, Y. Sun, Z. Yuan, Y. Tang, Pd nanochains: controlled synthesis by lysine and application in microbial fuel cells, *Chem. Eng. J.* 379 (2020), 122230, <https://doi.org/10.1016/j.cej.2019.122230>.
- [23] F. Wang, S. Wang, D. Wu, H. Huang, W. Yuan, L.Y. Zhang, Layered PdW nanosheet assemblies for alcohol electrooxidation, *Appl. Surf. Sci.* 537 (2021), 147860, <https://doi.org/10.1016/j.apsusc.2020.147860>.
- [24] Y. Zhang, X. Liu, T. Liu, X. Ma, Y. Feng, B. Xu, W. Cai, Y. Li, D. Su, Q. Shao, X. Huang, Rhombohedral Pd–Sb nanoplates with Pd-terminated surface: an efficient bifunctional fuel-cell catalyst, *Adv. Mater.* 34 (2022), 2202333, <https://doi.org/10.1002/adma.202202333>.
- [25] T. Wu, X. Wang, A. Emrehan Emre, J. Fan, Y. Min, Q. Xu, S. Sun, Graphene-nickel nitride hybrids supporting palladium nanoparticles for enhanced ethanol electrooxidation, *J. Energy Chem.* 55 (2021) 48–54, <https://doi.org/10.1016/j.ijechem.2020.06.056>.
- [26] W. Huang, X.Y. Ma, H. Wang, R. Feng, J. Zhou, P.N. Duchesne, P. Zhang, F. Chen, N. Han, F. Zhao, J. Zhou, W.B. Cai, Y. Li, Promoting effect of Ni(OH)₂ on palladium nanocrystals leads to greatly improved operation durability for electrocatalytic ethanol oxidation in alkaline solution, *Adv. Mater.* 29 (2017), 1703057, <https://doi.org/10.1002/adma.201703057>.
- [27] Z. Chen, J. Zhang, Y. Zhang, Y. Liu, X. Han, C. Zhong, W. Hu, Y. Deng, NiO-induced synthesis of PdNi bimetallic hollow nanocrystals with enhanced electrocatalytic activities toward ethanol and formic acid oxidation, *Nano Energy* 42 (2017) 353–362, <https://doi.org/10.1016/j.nanoen.2017.11.033>.
- [28] Y. Yang, J. Ren, Q. Li, Z. Zhou, S. Sun, W. Cai, Electrocatalysis of ethanol on a Pd electrode in alkaline media: an in situ attenuated total reflection surface-enhanced

- infrared absorption spectroscopy study, *ACS Catal.* 4 (2014) 798–803, <https://doi.org/10.1021/cs401198t>.
- [29] Z. Liang, T. Zhao, J. Xu, L. Zhu, Mechanism study of the ethanol oxidation reaction on palladium in alkaline media, *Electrochim. Acta* 54 (2009) 2203–2208, <https://doi.org/10.1016/j.electacta.2008.10.034>.
- [30] M. Wang, L. Li, M. Wang, X. Huang, Recent progress in palladium-nonmetal nanostructure development for fuel cell applications, *NPG Asia Mater.* 14 (2022), 78, <https://doi.org/10.1038/s41427-022-00423-2>.
- [31] J. Wang, Y. Kang, H. Yang, W. Cai, Boron-doped palladium nanoparticles on carbon black as a superior catalyst for formic acid electro-oxidation, *J. Phys. Chem. C* 113 (2009) 8366–8372, <https://doi.org/10.1021/jp900349g>.
- [32] Q. Zhang, J. Weng, J. Xu, Palladium phosphide/black phosphorus heterostructures with enhanced ethanol oxidation activity and stability, *J. Phys. Chem. C* 125 (2021) 18717–18724, <https://doi.org/10.1021/acs.jpcc.1c04550>.
- [33] L. Luo, C. Fu, F. Yang, X. Li, F. Jiang, Y. Guo, F. Zhu, L. Yang, S. Shen, J. Zhang, Composition-Graded Cu–Pd nanospheres with Ir-Doped surfaces on N-doped porous graphene for highly efficient ethanol electro-oxidation in alkaline media, *ACS Catal.* 10 (2019) 1171–1184, <https://doi.org/10.1021/acscatal.9b05292>.
- [34] L. Luo, C. Fu, S. Shen, F. Zhu, J. Zhang, Probing structure-designed Cu–Pd nanospheres and their Pt-monolayer-shell derivatives as high-performance electrocatalysts for alkaline and acidic oxygen reduction reactions, *J. Mater. Chem. A* 8 (2020) 22389–22400, <https://doi.org/10.1039/d0ta05905f>.
- [35] L. Luo, C. Fu, X. Yan, S. Shen, F. Yang, Y. Guo, F. Zhu, L. Yang, J. Zhang, Promoting effects of Au submonolayer shells on structure-designed Cu–Pd/Ir nanospheres: greatly enhanced activity and durability for alkaline ethanol electro-oxidation, *ACS Appl. Mater. Interfaces* 12 (2020) 25961–25971, <https://doi.org/10.1021/acsami.0c05605>.
- [36] L. Luo, Z. Tan, C. Fu, R. Xue, X. Cheng, T. Bi, L. Zhao, Y. Guo, X. Cai, J. Yin, S. Shen, J. Zhang, Shape-controlled synthesis of Pd nanotetrahedrons with Pt-doped surfaces for highly efficient electrocatalytic oxygen reduction and formic acid oxidation, *Chem. Eng. J.* 451 (2023), 138786, <https://doi.org/10.1016/j.cej.2022.138786>.
- [37] Z. Yu, S. Lv, Q. Yao, N. Fang, Y. Xu, Q. Shao, C.W. Pao, J.F. Lee, G. Li, L.M. Yang, X. Huang, Low-coordinated Pd site within amorphous palladium selenide for active, selective, and stable H₂O₂ electrosynthesis, *Adv. Mater.* 35 (2022), 2208101, <https://doi.org/10.1002/adma.202208101>.
- [38] X. Hu, Z. Xiao, W. Wang, L. Bu, Z. An, S. Liu, C.-W. Pao, C. Zhan, Z. Hu, Z. Yang, Y. Wang, X. Huang, Platinum–lead–bismuth/platinum–bismuth core/shell nanoplate achieves complete dehydrogenation pathway for direct formic acid oxidation catalysis, *J. Am. Chem. Soc.* 145 (2023) 15109–15117, <https://doi.org/10.1021/jacs.3c00262>.
- [39] Y. Zhang, B. Huang, G. Luo, T. Sun, Y. Feng, Y. Wang, Y. Ma, Q. Shao, Y. Li, Z. Zhou, X. Huang, Atomically deviated Pd–Te nanoplates boost methanol-tolerant fuel cells, *Sci. Adv.* 6 (2020), eaba9731, <https://doi.org/10.1126/sciadv.aba9731>.
- [40] Y. Feng, H. Yang, Y. Zhang, X. Huang, L. Li, T. Cheng, Q. Shao, Te-doped Pd nanocrystal for electrochemical urea production by efficiently coupling carbon dioxide reduction with nitrite reduction, *Nano Lett.* 20 (2020) 8282–8289, <https://doi.org/10.1021/acs.nanolett.0c03400>.
- [41] B. Jiang, H. Xue, P. Wang, H. Du, Y. Kang, J. Zhao, S. Wang, W. Zhou, Z. Bian, H. Li, J. Henzie, Y. Yamauchi, Noble-metal-metalloid alloy architectures: mesoporous amorphous iridium-tellurium alloy for electrochemical N₂ reduction, *J. Am. Chem. Soc.* 145 (2023) 6079–6086, <https://doi.org/10.1021/jacs.2c10637>.
- [42] K. Wang, D. Liu, L. Liu, X. Li, H. Wu, Z. Sun, M. Li, A.S. Vasenko, S. Ding, F. Wang, C. Xiao, Isolated metalloid tellurium atomic cluster on nitrogen-doped carbon nanosheet for high-capacity rechargeable lithium–CO₂ battery, *Adv. Sci.* 10 (2023), e2205959, <https://doi.org/10.1002/adv.202205959>.
- [43] J. Zhang, J. Ye, Q. Fan, Y. Jiang, Y. Zhu, H. Li, Z. Cao, Q. Kuang, J. Cheng, J. Zheng, Z. Xie, Cyclic penta-twinned rhodium nanobranches as superior catalysts for ethanol electro-oxidation, *J. Am. Chem. Soc.* 140 (2018) 11232–11240, <https://doi.org/10.1021/jacs.8b03080>.
- [44] Z. Zhou, Q. Wang, J. Lin, N. Tian, S. Sun, In situ FTIR spectroscopic studies of electrooxidation of ethanol on Pd electrode in alkaline media, *Electrochim. Acta* 55 (2010) 7995–7999, <https://doi.org/10.1016/j.electacta.2010.02.071>.
- [45] M. Li, D. Cullen, K. Sasaki, N. Marinkovic, K. More, R. Adzic, Ternary electrocatalysts for oxidizing ethanol to carbon dioxide: making it capable of splitting C–C bond, *J. Am. Chem. Soc.* 135 (2013) 132–141, <https://doi.org/10.1021/ja306384x>.
- [46] M. Farsadrooh, J. Torrero, L. Pascual, M.A. Peña, M. Retuerto, S. Rojas, Two-dimensional Pd-nanosheets as efficient electrocatalysts for ethanol electrooxidation. Evidences of the C–C scission at low potentials, *Appl. Catal. B Environ.* 237 (2018) 866–875, <https://doi.org/10.1016/j.apcatb.2018.06.051>.
- [47] F. Lv, W. Zhang, M. Sun, F. Lin, T. Wu, P. Zhou, W. Yang, P. Gao, B. Huang, S. Guo, Au Clusters on Pd nanosheets selectively switch the pathway of ethanol electrooxidation: amorphous/crystalline interface matters, *Adv. Energy Mater.* 11 (2021), 2100187, <https://doi.org/10.1002/aenm.202100187>.
- [48] J. Ye, Y. Jiang, T. Sheng, S. Sun, In-situ FTIR spectroscopic studies of electrocatalytic reactions and processes, *Nano Energy* 29 (2016) 414–427, <https://doi.org/10.1016/j.nanoen.2016.06.023>.
- [49] M. Xie, B. Zhang, Z. Jin, P. Li, G. Yu, Atomically reconstructed palladium metallene by intercalation-induced lattice expansion and amorphization for highly efficient electrocatalysis, *ACS Nano* 16 (2022) 13715–13727, <https://doi.org/10.1021/acsnano.2c05190>.
- [50] Y. Chen, J. Pei, Z. Chen, A. Li, S. Ji, H. Rong, Q. Xu, T. Wang, A. Zhang, H. Tang, J. Zhu, X. Han, Z. Zhuang, G. Zhou, D. Wang, Pt atomic layers with tensile strain and rich defects boost ethanol electrooxidation, *Nano Lett.* 22 (2022) 7563–7571, <https://doi.org/10.1021/acs.nanolett.2c02572>.
- [51] Y. Guo, B. Li, S. Shen, L. Luo, G. Wang, J. Zhang, Potential-dependent mechanistic study of ethanol electro-oxidation on palladium, *ACS Appl. Mater. Interfaces* 13 (2021) 16602–16610, <https://doi.org/10.1021/acsami.1c04513>.